Wire arc additive manufacturing of Ni—Fe alloy/ductile cast iron bimetallic structure; phase transformations, microstructure and crystallographic texture

Mahmoudiniya, Mahdi; Thorr, Anne Sophie; Petrov, Roumen H.; Hermans, Marcel J.M.; Kestens, Leo A.I.

DOI
10.1016/j.matchar.2024.114650

Publication date
2025

Document Version
Final published version

Published in
Materials Characterization

Citation (APA)
Mahmoudiniya, M., Thorr, A. S., Petrov, R. H., Hermans, M. J. M., & Kestens, L. A. I. (2025). Wire arc additive manufacturing of Ni—Fe alloy/ductile cast iron bimetallic structure; phase transformations, microstructure and crystallographic texture. *Materials Characterization*, *220*, Article 114650. https://doi.org/10.1016/j.matchar.2024.114650

Materials Characterization 220 (2025) 114650

Contents lists available at ScienceDirect

Materials Characterization

journal homepage: www.elsevier.com/locate/matchar

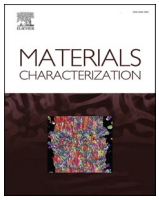

Wire arc additive manufacturing of Ni—Fe alloy/ductile cast iron bimetallic structure; phase transformations, microstructure and crystallographic texture

Mahdi Mahmoudiniya [a,*], Anne-Sophie Thorr [b], Roumen H. Petrov [a,c], Marcel J.M. Hermans [c], Leo A.I. Kestens [a,c]

[a] Ghent University, Metals Science and Technology Group, Technologiepark 903 B-9052 Zwijnaarde, Ghent, Belgium
[b] Naval Group, Technocampus Ocean, 5 rue de l'Halbrane, Bouguenais, France
[c] Delft University of Technology, Department of Materials Science and Engineering, Mekelweg, 22628, CD, Delft, the Netherlands

ARTICLE INFO

Keywords:
Bimetallic components
Wire arc additive manufacturing
Ductile cast iron
Crystallographic texture
Interfacial microstructure, Profilometry-based indentation plastometry

ABSTRACT

Wire arc additive manufacturing (WAAM) is a significant area of interest within the field of additive manufacturing (AM). In the present research, WAAM technology was employed to deposit a Ni-based alloy on a ductile cast iron substrate to fabricate a bimetallic structure of Ni-45 %Fe alloy and ductile cast iron. Scanning electron microscopy (SEM), energy dispersive spectroscopy (EDS), electron back scattered diffraction (EBSD) and X-ray diffraction (XRD) were used to study phase transformations, microstructure and crystallographic texture development in interfacial regions as well as deposited material. The mechanical properties were also studied using micro-hardness and profilometry-based indentation plastometry (PIP) measurements. The results showed that a wide variety of phases are generated within the heat-affected zone (HAZ) and partially melted zone (PMZ). These phases form complex microstructures with single and double shell morphology. The deposited alloy has a face-centred cubic (FCC) structure, with some carbides and graphite that are formed during the solidification of the first deposited layer. The compositional changes were also observed across the interface. The texture of the deposited alloy showed around 30° deviation from ⟨100⟩ II building direction due to the shape and overlap of the melt pools. The present results provide a better understanding of interface development mechanisms during WAAM of bimetallic structures. The peak of the hardness across the interface was observed in PMZ because of the formation of a martensitic matrix. The PIP measurements showed that the σ_y and the UTS of deposited alloy are lower than the cast iron base metal.

1. Introduction

Cast irons are a group of ferrous alloys containing carbon (more than 2 %) and silicon (1 to 3 %) as main alloying elements together with small amounts of elements that are usually present in Fe-based alloys, like Mn, S and P. Considering the wide range of alloying elements and processing routes, different groups of cast irons with a wide variety of properties can be produced, including: grey cast iron, white cast iron, malleable cast iron and ductile cast iron [1]. Ductile cast irons, also known as nodular or spheroidal graphite (SG) irons, are among the most used ones in recent years. The presence of discrete nodular or spheroidal graphite produces unique properties such as high strength, reasonable toughness and excellent fatigue strength [2]. Hybrid metal parts containing ductile cast iron as the substrate could be a suitable candidate for some applications like the die and mold manufacturing industry. In this regards, additive manufacturing is considered a promising method to produce hybrid parts. Wire arc additive manufacturing, among different AM techniques, is considered one of the most cost-effective manufacturing methods, especially for small series. Additionally, the high deposition rate during WAAM has made this technique suitable for producing medium to large parts [3]. Accordingly, WAAM has been implemented for a wide variety of metals and alloys, such as steels [4] [5], Al alloys [6], superalloys [7], and Ti alloys [8]. One of the important capabilities of WAAM is the potential to produce large bimetallic structures, especially when the high production rate is one of the main requirements. These bimetallic parts can be produced in two main scenarios: i) the

* Corresponding author.
E-mail address: mahdi.mahmoudiniya@Ugent.be (M. Mahmoudiniya).

https://doi.org/10.1016/j.matchar.2024.114650
Received 25 October 2023; Received in revised form 19 July 2024; Accepted 12 December 2024
Available online 15 December 2024

entire bimetallic part is additively produced using WAAM, and ii) one part is additively printed on a substrate from a different metal, which has been fabricated using conventional methods. Different bimetallic components such as NiTi/316 L [9], 316 L/low carbon steel [10], nickel aluminium bronze/ 316 L [11], and Inconel 718/Steel S275 [12] have been produced using WAAM. So far, no attempt has been made to produce ductile cast irons using AM techniques. It might be because i) creating the complex microstructure of a ductile cast iron using available AM techniques is challenging, and ii) as the casting of ductile cast irons is a cost-competitive method, there is virtually no demand for the production of this alloy using AM techniques. Accordingly, printing the desired part on a conventionally manufactured ductile cast iron would be the only possible scenario for producing hybrid metal parts containing ductile cast iron. In this regard, Park et al. [13] have recently used the direct laser energy deposition method to repair a ductile cast iron part using powders of a high manganese steel. Sebastian et al. [13] have printed a part of Inconel 625 alloy, with a thickness of 200 mm, on a grey cast iron substrate using the Selective Laser Melting (SLM) technique. They studied the microstructural and compositional changes across the interface between the substrate and deposited material. Ni—Fe alloys can be used to coat ductile cast irons, creating Ni-Fe/ductile cast iron hybrid components. This hybrid component has potential applications in various areas, including the following. Considering the good corrosion resistance of Ni—Fe alloys and the low cost of the ductile cast irons, this structure can be considered to manufacture a cost-effective corrosion-resistant structure. This strategy has also been used by Samantaray et al. [14], who deposited a corrosion resistance layer of supper alloy on top of steel. In the present study, the hybrid structure under investigation will serve as the initial configuration for producing a plastic injection mold. The surface layer of the injection mold should be highly wear and heat-resistant. The resistant layers cannot be directly deposited on the cast iron due to physical and chemical incompatibilities. In this case, the deposited Ni—Fe alloy acts as an appropriate intermediate layer between the resistant layer and the cast iron because of its low thermal expansion to accommodate thermal stresses and favourable metallurgical compatibility with cast irons. It should be noted that Ni-based fillers or electrodes are amply used for the welding of cast irons as the molten Ni rejects the absorbed carbon from the cast iron as graphite. The formation of graphite increases the volume of the deposited weld and reduces the shrinkage stresses, and, in turn, decreases the likelihood of cracking. There are studies on the usage of WAAM for producing Ni—Fe alloys. For example, Veiga et al. [15] produced FeNi36 alloy using plasma arc welding and gas tungsten arc welding and then compared mechanical properties. Recently, Sood et al. [16] utilised WAAM technology to manufacture walls of Invar 36 alloy with varying heat inputs. They also examined the thermal and mechanical properties of the produced walls in different directions. However, previous studies have only focused on producing mono-materials of Ni—Fe alloys without any interface in the final product. To the authors' best knowledge, no study has been reported on using WAAM to fabricate Ni—Fe alloy/ductile cast iron hybrid components. Considering previous works on AM of bimetallic components, fabrication of such components is usually accompanied by the formation of microstructural gradients, especially across the interface. Studying this microstructural gradient is crucial as it determines the final properties and performance of the manufactured hybrid part. The complex physical and chemical interactions in the interface region result in the formation of a complex microstructure across the interface, which is challenging to study. This microstructure tends to be more complicated where the substrate or deposited material exhibits an intricately complex microstructure such as is the case for ductile cast irons. This complexity may originate from subsequent phase transformations, in both liquid and solid-state, occurring during cooling. Accordingly, our goal in this project is to examine the process of depositing a Ni-45 %Fe alloy on a ductile cast iron substrate to create a bimetallic component using WAAM. The study provides a better understanding of microstructure and texture development in the interface and deposited material, which can help in the development of bimetallic components containing ductile cast irons. It should be noted that the Ni-45 %Fe alloy is a Ni-based alloy with characteristics like high strength, good ductility and low thermal expansion [17]. This alloy can be used for cladding, repairing, and welding ductile cast irons [18].

2. Experimental procedure

2.1. Materials and WAAM process

A block of EN-GJS-500-7 cast iron, with 200 mm × 200 mm × 30 mm dimensions and a wire of Ni- 45 %Fe alloy, having a diameter of 1.2 mm, were used as substrate and feed stock material, respectively.

Table 1 summarizes the nominal chemical compositions.

The deposition process was carried out using a cold metal transfer (CMT) welding system via a Fronius CMT TPS4000 machine under the welding conditions summarized in Table 2. A mixture of Ar-35 %He-2 % CO_2 was used as the shielding gas during the deposition process to protect the melt and the electrode. The preheat temperature of 170 °C was set for the cast iron substrate.

A 20 mm-thick block with dimensions 100 mm × 100 mm was deposited through a bidirectional scanning strategy. Fig. 1 depicts more details about the dimensions of the fabricated hybrid part, the scan strategy used for the deposition process, and the top-view image of the processed part.

2.2. Microstructural characterization

The manufactured part was sectioned parallel to plane of Transverse Direction - Building Direction (TD-BD) and Welding/deposition Direction-Building Direction (WD-BD) to analyze the macro and microstructure. A standard metallographic procedure, including grinding and polishing, was followed to prepare samples for optical and scanning electron microscopy observations. The etchants of Nital4% and Aqua Regia (10 ml HNO_3 + 40 mL HCl) were used to reveal the microstructure of cast iron and deposited layers, respectively.

For EBSD measurements, the OPU solution was used as the final polishing step to prepare the surface of the samples. The EBSD measurements were carried out using a scanning electron microscope equipped with a Field Emmission Gun (Quanta 450 FEG-SEM). The orientation data were acquired with OIM DC v.7.31 in a hexagonal scan grit scanning mode. The EBSD scans were recorded with an acceleration voltage of 20 kV and a probe current of ~2.3 nA. The collected data were processed with the OIM 8.6 software. Additionally, phase analysis was carried out using the conventional X-ray diffraction (XRD) method with a copper Kα tube and the scan step size of 0.02 degrees over the 2θ range from 30 to 110°. The XRD diffractometer was operated at a current of 40 mA and 40 kV.

2.3. Mechanical properties

To measure the hardness profile for the bimetallic structure, a Vickers microhardness tester was used with a 200 g load. Three measurements were taken and then averaged for each height build. The stress-strain relationship of different regions of the resultant bimetallic structure was investigated using profilometry-based indentation

Table 1
Chemical composition of substrate and wire used in the present study.

Material	Wt% of alloying elements						
	C	Si	Mn	P	S	Ni	Fe
Cast Iron substrate	3.4–3.85	2.3–3.1	0.1–0.3	< 0.1	<0.02	–	Bal
Ni-Fe Wire	0.05	0.14	0.83	–	–	55	Bal

Table 2
The WAAM process parameters.

Arc current (A)	Arc voltage (V)	Welding speed (mm/min)	Shield gas flow rate (L/min)	Layer thickness (mm)	Hatching distance (mm)	Diameter of the wire (mm)	Wire feeding speed (m/min)	Deposition rate (gr/h)	Contact tip to workpiece distance (mm)
220	20.1	1000	14–16	2.5	3.25	1.2	7	3900	17

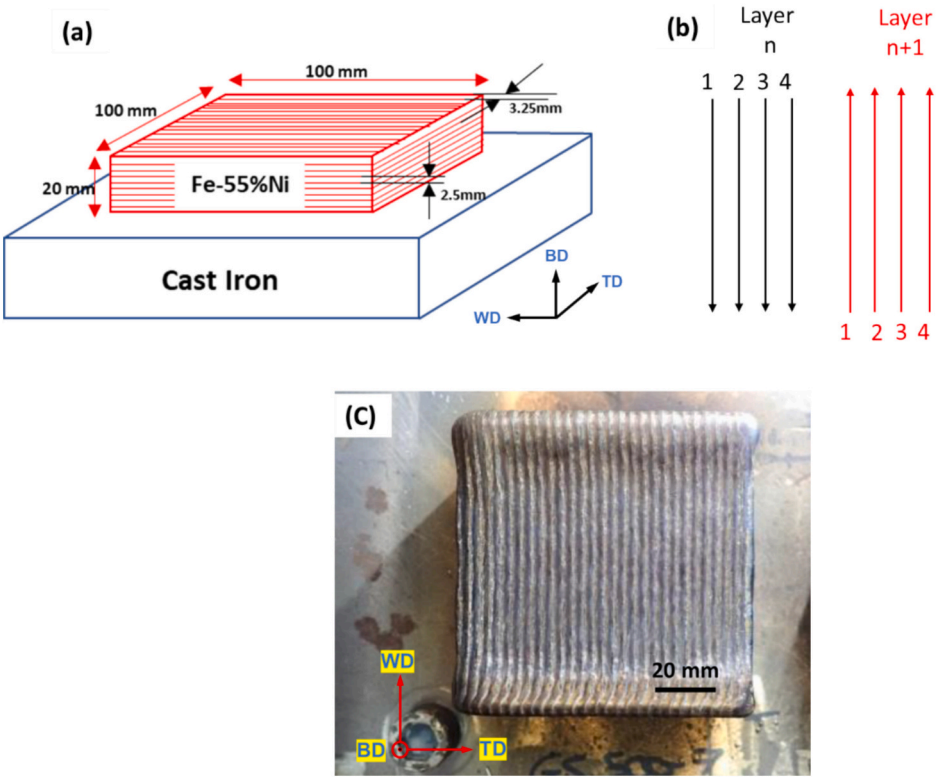

Fig. 1. (a) Geometry of the fabricated part, (b) scan strategy of the deposition process and (c) topview image of the final part, WD is the welding direction, TD is the transverse direction and BD is the building direction.

plastometry (PIP) methodology. The PIP procedure consists of different steps, including (i) pushing an indent to the surface of the sample, (ii) profilometry of the indent, and (iii) running iterative finite element method (FEM) based simulation to find a best-fit set of (Voce) plasticity parameter values [19]. Then, the true stress – true strain relationship is converted to a nominal stress - nominal strain relationship for tensile testing. In the current research, a spherical indenter of radius 0.503 mm, made of Si_3N_4, was employed to indent the different regions of the sample in the TD-BD plane.

3. Results

3.1. Macrostructural observations

Fig. 2 depicts low magnification optical microscopy images of the built part, etched by Aqua Regia, revealing the interface between the cast iron substrate and deposited Fe—Ni alloy in the TD-BD and WD-BD planes.

It is observed from the TD-BD micrograph that each layer is composed of successively deposited tracks next to each other. The melt pool boundaries are also visible as the bright-etched boundaries in the TD-BD plane. The different chemical composition of these lines is probably responsible for different etching behaviours [20]. The melt pools overlap with each other and they have similar shape in the different layers. The mean distance between the adjacent melt pools is about 3.2 mm. Some cracks are observed in the deposited layers. It

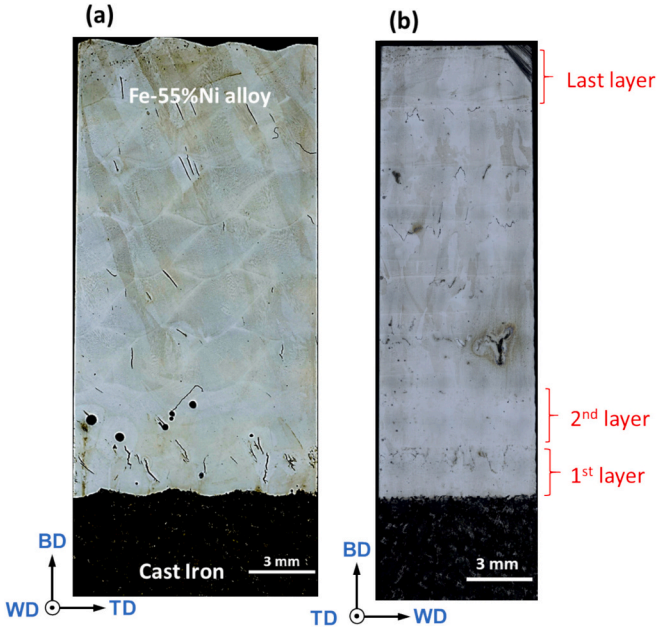

Fig. 2. Low magnification optical images of the deposited layers in different sections.

seems that more cracks have been formed in the first deposited layer than in the subsequent layers. Fig. 3 shows optical microscopy images of the formed cracks. In addition, spherical pores are observed mainly in the first and second deposited layers (c.f Fig. 3a). The size distribution of these porosities is illustrated in Fig. 3d. It is seen that the diameter of most porosities falls within the range of 100 to 400 μm, with a peak of around 250 μm. The formation of these pores can be ascribed to trapped gas, mainly hydrogen, in the weld/deposited metal after solidification [21]. Hydrogen can be generated from various sources, such as moisture, grease, and hydrocarbon impurities on the wire and base plate surfaces. The electric arc vaporises impurities, generating atomic hydrogen that gets absorbed into the molten pool and ultimately trapped during solidification [22]. It should be noted that most of these pores have been formed near the fusion boundaries. This is likely due to the higher concentration of hydrogen sources on the surface of the cast iron. It is observed that from the second deposited layer upwards, most of the cracks are formed underneath the melt pool boundaries (cf Fig. 3b and c), i.e. in the heat affected zone in the prior deposited bead. It is seen that most cracks have the same orientation with regard to BD. This directionality of the cracks is related to the heat extract direction.

3.2. Microstructural development

3.2.1. Base material

Fig. 4 shows the microstructure of the cast iron substrate, which consists of a pearlitic matrix with graphite nodules and some large cementite particles (red arrows). The presence of some cementite particles is related to high undercooling during solidification, resulting in a high growth rate of the cementite which is comparable to that of the graphite [23].

3.2.2. Interfacial regions

Fig. 5 presents the microstructure, revealed by 5 % Nital, at the interfacial area between the substrate and the deposited alloy. The region between the ductile cast iron substrate and the deposited alloy contains two specific zones *(i)* a heat-affected zone (HAZ) and *(ii)* a partially melted zone (PMZ). The microstructure of each zone will be described later.

Fig. 6 shows the microstructure of the HAZ that is composed of preexisting graphite nodules (Gr) and preexisting cementite particles embedded into a pearlitic-like matrix.

Further analysis of images across the HAZ/substrate interface at high magnification, cf. Fig. 7a and b, reveal that the microstructure of the matrix in the HAZ is somewhat different from the pearlite matrix of the cast iron base metal. Fig. 7c and d depict different microstructures, including ferrite (F), retained austenite (RA), martensite (M), in combination with a fine pearlitic structure that have been formed between the cementite lamellas in the matrix of the HAZ. Additionally, Fig. 7e shows that in some regions of the HAZ, the pearlitic cementite is spheroidized.

The microstructure of the PMZ is shown in Fig. 8. It is observed that the microstructure in the lower parts of the PMZ, close to the HAZ, is different from the upper parts of the PMZ (cf. Fig. 8a). In the lower part, the microstructure is composed of a martensitic (or tempered

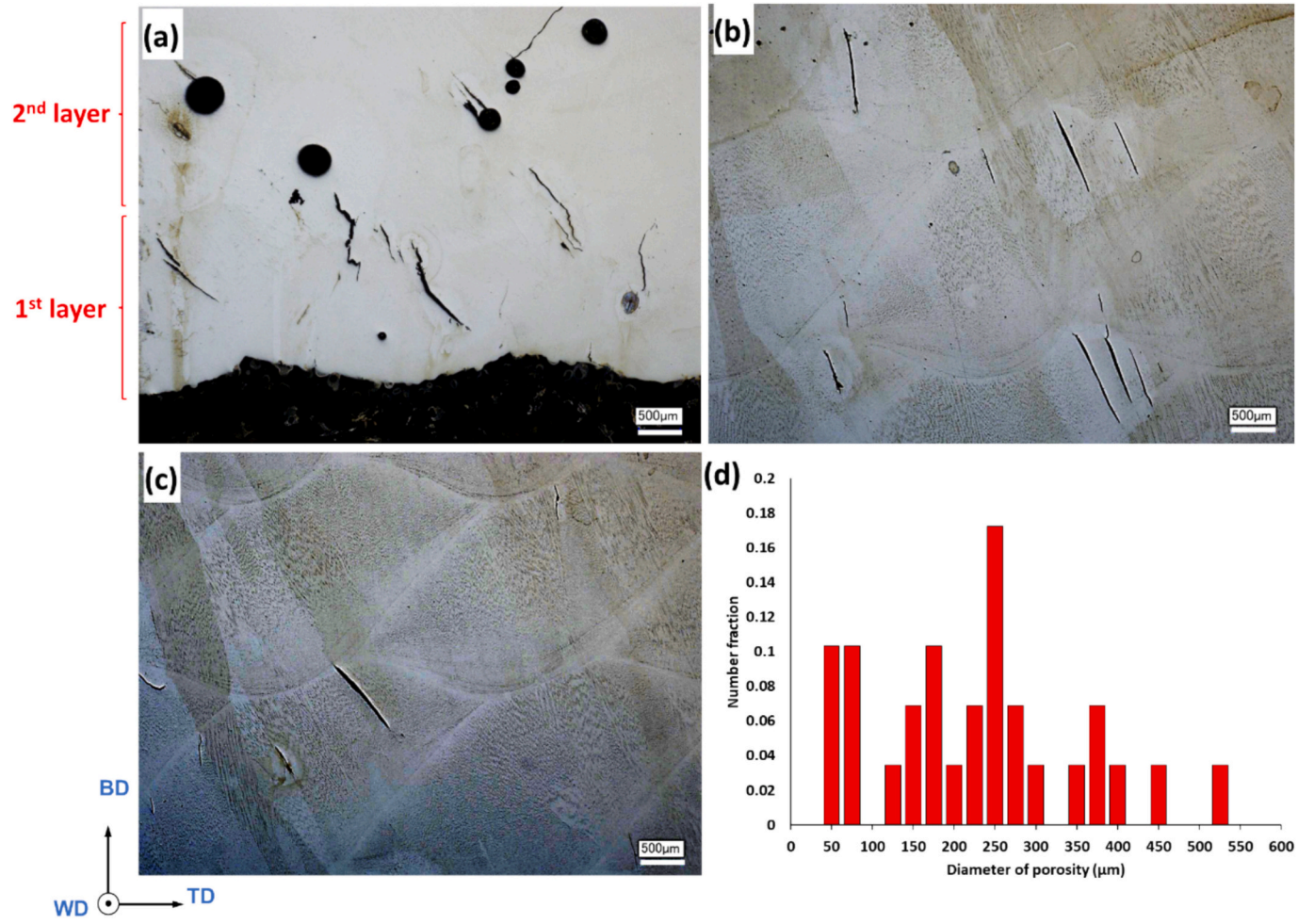

Fig. 3. Formation of some defects during fabrication of a bimetallic structure in the (a) first and second deposited layers, (b) and (c) following layers, (d) diameter distribution of porosities observed in deposited layers.

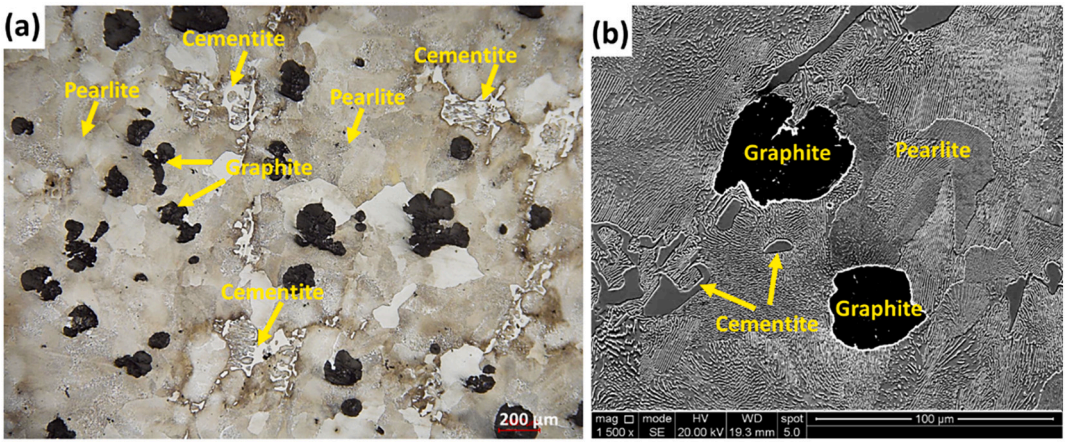

Fig. 4. The microstructure of the ductile cast iron substrate: (a) the optical micrograph and (b) the secondary electron (SE) -SEM image. The red arrows indicate the eutecticum containing cementite particles and pearlite.
(For interpretation of the references to colour in this figure legend, the reader is referred to the web version of this article.)

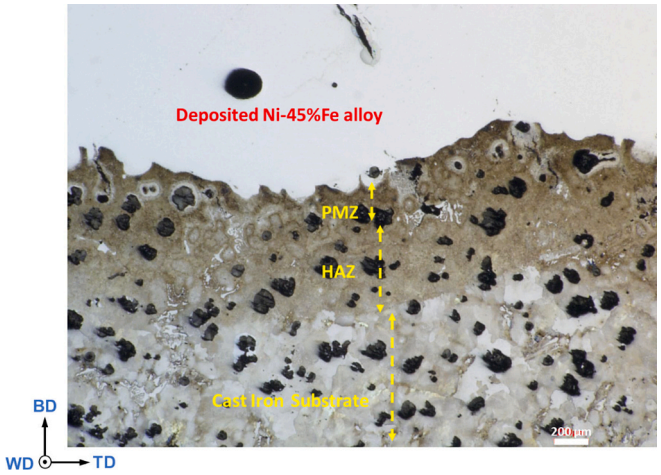

Fig. 5. The optical micrograph of the interfacial region between the substrate and deposited alloy.

martensite) matrix within which some graphite nodules and cementite particles are still present.

As shown in Fig. 8a, in the upper PMZ, the microstructure around the graphite nodules differs from the martensitic matrix, where different shells surround the graphite particles. Fig. 9 reveals further details of these different microstructures. Furthermore, some cracks are also observed in the upper region of the PMZ, cf. Fig. 8a.

Regarding Fig. 9b and e, the first shell around the graphite nodule has a martensitic (Fig. 9b) or bainitic (Fig. 9e) microstructure, while the outer shell consists of transformed ledeburite, cf. Fig. 9f and g. It should be noted that the ledeburite is composed of cementite and austenite phases formed during the eutectic reaction [17]. However, the austenite might transform into other products during cooling to room temperature. In some regions of the upper PMZ, it is observed that only a transformed ledeburite shell surrounds graphite nodules, cf Fig. 10a. Moreover, in some areas the graphite nodules are completely transformed into the ledeburite (L), cf. Fig. 10b and c.

Fig. 11 shows SEM images of the microstructural changes across the boundary between the PMZ and deposited layer. A narrow layer, indicated by the red arrows in Fig. 11b, has a thickness of around 12 µm, is just adjacent to the PMZ. In regions above this layer, different phases arranged in various structural constituents can be observed (yellow and blue arrows in Fig. 11b). The yellow arrows indicate cementite

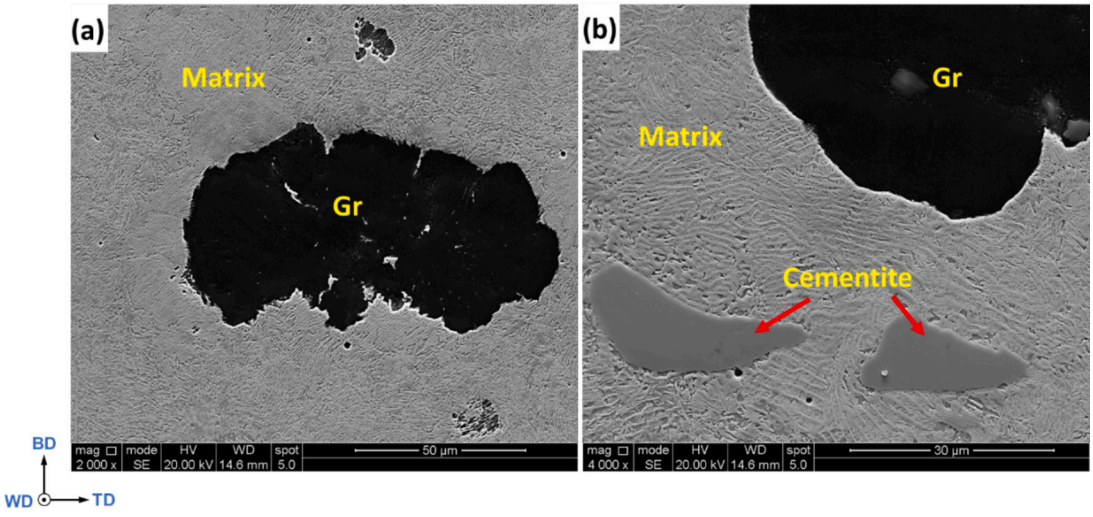

Fig. 6. SEM images of the microstructure of the HAZ on the ductile cast iron side showing: (a) graphite embedded in pearlitic matrix, and (b) cementite and graphite in pearlitic matrix.

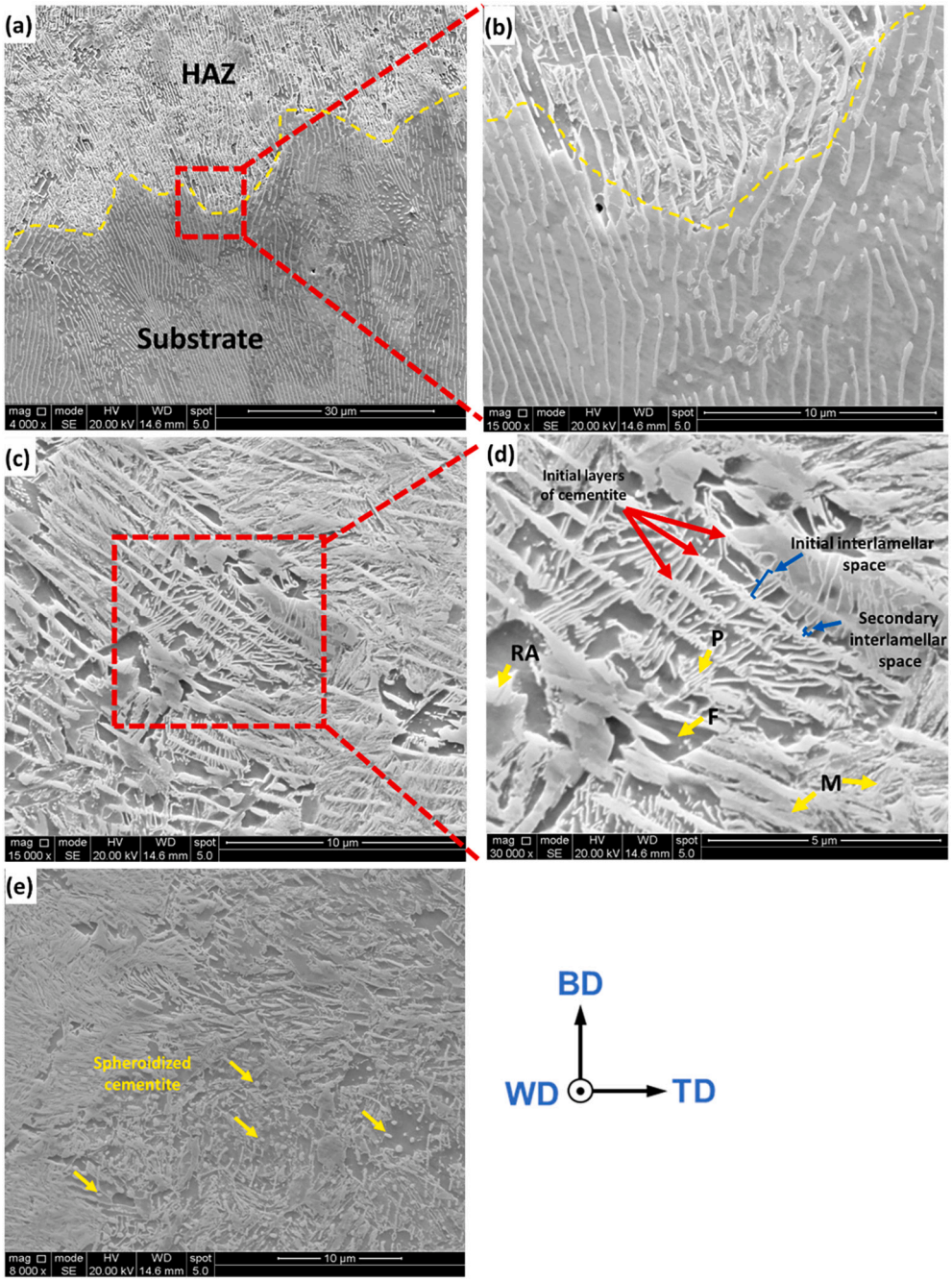

Fig. 7. (a) and (b) the microstructural changes across the base metal/HAZ boundary, (c) and (d) the microstructure of the matrix of HAZ having different phases (M: Martensite, F: Ferrite, P: Pearlite and RA: Retained austenite) and (e): cementite spheroidization in the HAZ.

networks, while the black dots, marked with blue arrows, are graphite particles. To obtain additional information, the EBSD scan was conducted on the area indicated by the yellow square in Fig. 11b and the results are shown in Fig. 12. The phase map, cf. Fig. 12c, shows that the thin layer in the deposited material next to the PMZ is an FCC phase followed by a layer of cementite as a result of eutectic decomposition [24].

The distribution of the main alloying elements across the interface is shown in Fig. 12, d, e and f. The Ni concentration is gradually increased from PMZ to the deposited layer, while the Fe and Si distribution shows an inverse trend. These changes are observed first in the thin layer corresponding to the zone marked with red arrows in Fig. 11b. The C map also confirms that some graphite particles have been solidified from the liquid during solidification. Within the sensitivity limits of the EDX technique (~0.1 wt%), no significant changes in Mn distribution were observed across the interface. Furthermore, the BD-inverse pole figure (IPF) and phase maps, Fig. 12b and c, show that the microstructure of the matrix in the PMZ consists of plate martensite (green coloured) as well as retained austenite (red coloured).

The XRD results, shown in Fig. 13, additionally confirmed that the deposited layer has a single phase austenitic structure.

Fig. 14 illustrates the microstructure of different deposited layers. In the first deposited layer, cf. Fig. 14a and b, some equiaxed grains have been formed on top of the interface, indicating the narrow layer observed in Fig. 12. Afterwards, the columnar morphology of the grains is apparent, revealing the preferential growth whereby the grains are elongated perpendicular to the interface within the first deposited layer. The melt pool boundaries (yellow dashed lines) are marked by a

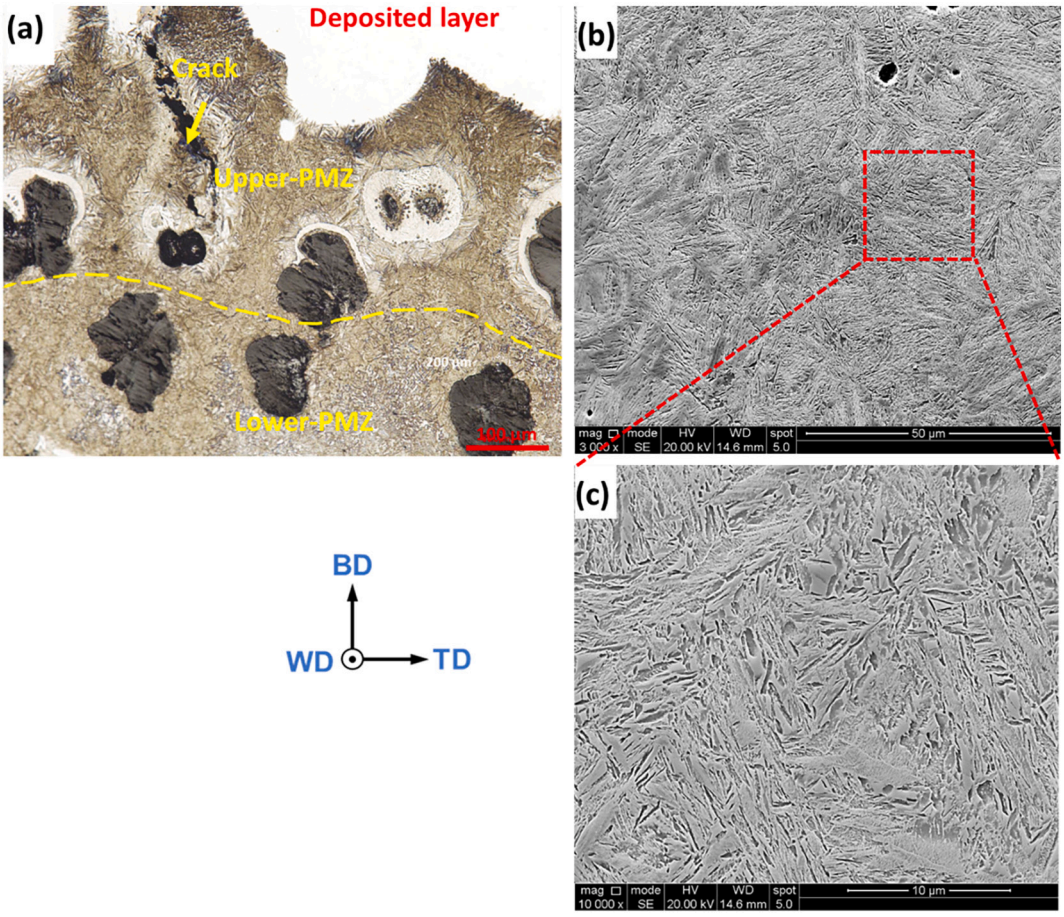

Fig. 8. (a) The microstructure of PMZ, (b) and (c) the matrix of PMZ.

discontinuous change in solidification direction. Apparently, the grains are elongated perpendicular to the interface of the melt pool boundary. For the following deposited layers, it is seen that the coarse and elongated grains dominate the microstructure, cf. Fig. 14d and f. Additionally, the SEM images reveal a cellular type of microstructure. The melt pool boundaries have been marked with yellow dashed lines in SEM images (cf. Fig. 14c and e). As can be seen, the melt pool boundaries are not visible in IPF maps for the 4th and last deposited layers, indicating that the crystals keep their orientations across the melt pool boundaries. It is worth noting that grains have been elongated with a deviation of around 20° to the building direction.

The size and shape of the developed grains were also analyzed using the EBSD results, see Fig. 15.

The EBSD post-processing software allows to calculate for each grain the grain aspect ration (ϕ), by approximating each grain by an ellips with minor axis L_1 and major axis L_2, whereby $\phi = L_1/L_2$ [25]. The grains having $\phi < 0.33$ are considered columnar, while those with $\phi \geq 0.33$ are considered equiaxed grains [26]. Analyzing the distributions of grain aspect ratio revealed that 77 % of the grains in the first layer have solidified with a columnar morphology, and the rest developed with an equiaxed morphology. The columnar morphology for the 4th and last deposited layers reaches 33 % and 97 %, respectively. The decreasing area fraction of the grains with columnar morphology in the 4th layer is attributed to the limited number of scanned grains during EBSD measurement because of the large grain size. For the first layer, the length of minor axes varies to less than ~220 µm, while for the 4th and last deposited layer it reaches ~800 µm and ~550 µm, respectively. The size distribution of the major axes reveals that there are no grains with $L_2 >$ ~1100 µm in the first layer, while the distribution range extends to $L_2 >$ ~1600 and ~1900 µm for the 4th and final deposited layer, respectively. The grain area was also calculated to analyze the grain size, as shown in Fig. 15d. The grain areas of 0.12×10^6, 2.6×10^6 and 1.3×10^6 µm^2 were measured for the first, 4th and last deposited layers, respectively, indicating the coarsening of the microstructure after deposition of the first layer. The decrease of the grain area in the last deposited layer is because of the formation of smaller grains in the highest region of the layer which remelt when a subsequent bead is deposited. This smaller grains re marked by black arrows in Fig. 14b.

Fig. 16 illustrates the micro-texture results for different deposited layers. The pole figures (PFs) were calculated with series rank (L) = 16, Gaussian half-width of 7° and triclinic sample symmetry. As the PFs show, the maximum intensity increases by increasing the number of solidified layers, indicating texture strengthening as the deposition process advances from the interface to the final solidified layer. It should be noted that the observed texture sharpening is related to the increased grain size. In view of the limited field width of the scanning, the presented PFs do not reveal any sample symmetry, which may be the result of poor scanning statistics. To observe the sample symmetry induced by the WAAM process, a higher number of melt pools should be scanned; considering the large area of the melt pool in WAAM, scanning such area with sufficient field width would be challenging. It is seen from Fig. 16, that in all different layers, the maximum intensity belongs to the (100) and (111) pole figures. It is evident that <100> II BD is the predominant texture in all analyzed layers. However, a deviation of about 30° from the BD can be seen in (100) PFs.

3.3. Mechanical properties

Fig. 17 shows the hardness profile of the bimetallic structure across

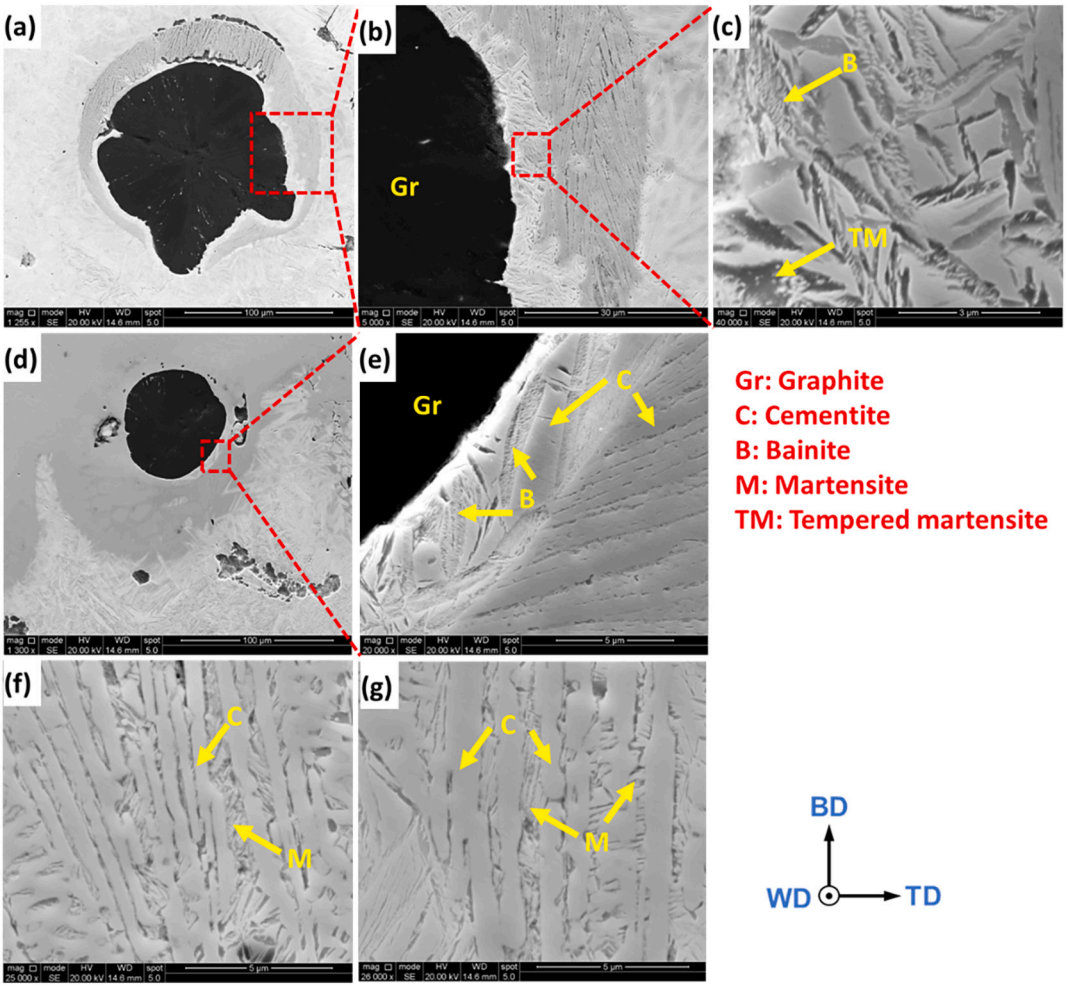

Fig. 9. SEM images of the microstructure around the graphite nodules in the upper region of PMZ, (a) to (c): martensite and ledeburite, (d) and (e): bainite and ledeburite, (f) and (g) The microstructure of ledeburite around graphite nodules.

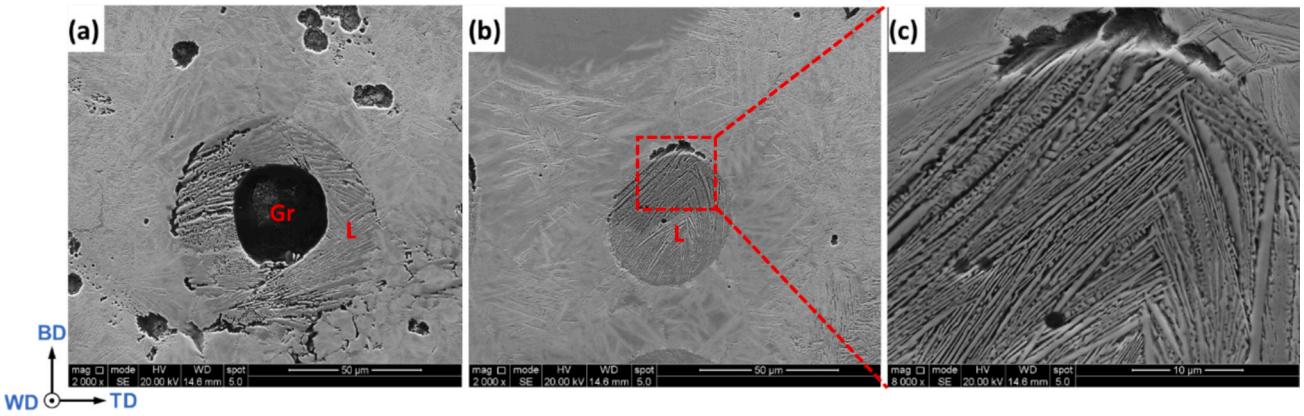

Fig. 10. The microstructure of PMZ (a): surrounding graphite with only ledeborite (L), (b) and (c): the complete transformation of graphite to ledeburite during solidification.

the interface where the hardness distinction between both sides of the interface is obvious. On the cast iron side, hardness increases by 26 % from 250 to 317 HV by moving from the substrate toward the HAZ. Then, It reaches the maximum value of 437 HV in the PMZ. On the Ni—Fe alloy side, there is a significant decrease of 60 % to 178 HV upon entering the deposited region. After that, the hardness experiences a further 11 % reduction and then remains constant along the height of the build.

Fig. 18 shows the nominal stress-strain curves obtained from PIP measurements corresponding to different regions of the BD-TD section. The calculated properties are also summarized in Table 3.

About the PIP measurements, it is noticeable that to simulate the deformation process using iterative finite element simulation; first, the true stress-strain relationship is characterized using the Voce law in the

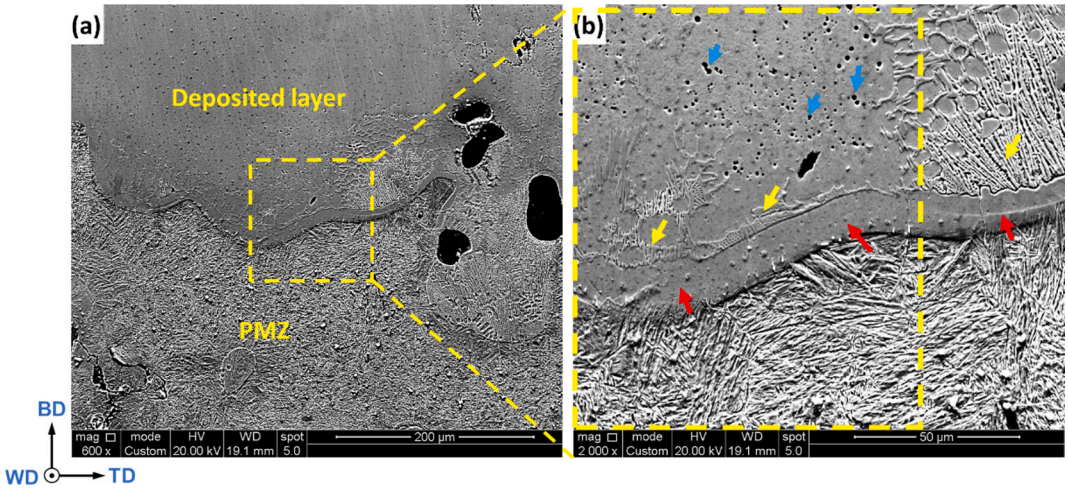

Fig. 11. (a) SEM image of microstructural changes across the interfacial region between PMZ and deposited material and (b) enlargement of the yellow dashed zone in Fig. 11a. (For interpretation of the references to colour in this figure legend, the reader is referred to the web version of this article.)

following form:

$$\sigma = \sigma_s - (\sigma_s - \sigma_Y) exp\left(\frac{-\varepsilon}{\varepsilon_0}\right) \quad (1)$$

where σ, ε, σ_Y, σ_s and ε_0 are true stress, true strain, yield stress, saturation stress and characteristic strain, respectively. After evaluating the Voce constitutive law parameters, the stress-strain curve can be plotted both as a true stress-strain curve or as a nominal stress-strain curve. The nominal stress (σ_N) and strain (ε_N) are calculated as:

$$\sigma_N = \frac{\sigma_T}{(1+\varepsilon_N)} \quad (2)$$

$$\varepsilon_N = exp(\varepsilon_T) - 1 \quad (3)$$

where the σ_T and ε_T are true stress and true strain, respectively. It is noticeable that the nominal stress-strain curve obtained in this way is only valid while the stress and strain fields within the gauge length of the sample are uniform. Compared to the properties of the as-welded Ni—Fe alloy reported by the supplier data sheet, the regions of the deposited alloy revealed lower σ_y and higher *UTS*. It is seen that σ_y of the deposited alloy is nearly the same at points 1 and 2. Although, the deposited material at point 1 (the build height of 6.2 mm) showed a 7.8 % higher UTS than the materials at point 2 (the build height of 16.4 mm). The uniform elongation of the deposited material was lower than what was reported by the supplier datasheet.

4. Discussion

The microstructural characterization reveals the formation of a complicated microstructure across the interface during WAAM deposition of Ni-45 %Fe alloy on a ductile cast iron substrate. These complexities mainly arise from *(i)* the formation of various phases due to different phase transformations occurring during (rapid) heating and cooling of ductile cast iron, *(ii)* local reponse to complex thermal cycles associated with WAAM, and *(iii)* compositional changes due to melting of the cast iron substrate and mixing with the deposited material in the first deposited layer. This complexity predominantly appears within three distinct regions of HAZ, PMZ and the first deposited layer. The HAZ is the first region where changes in the substrate's microstructure are observed. In this region, the initial microstructure only experiences heating and cooling cycles, and the temperature does not exceed Ac_3. The main observable effect is that cementite lamellas of the pearlitic matrix begin to dissolve and release carbon to the surrounding regions. The partitioning of carbon into the matrix is necessary to dissolve pre-existing cementite. Because of the high heating and cooling rates in the HAZ, there is not enough time for cementite to be completely dissolved. The partially dissolved cementite can be observed as thinned layers of cementite or spheroidized carbides, cf. Fig. 7. It was also shown that the graphite nodules and initial large distributed cementite have remained unchanged in HAZ, suggesting that the thermal condition for releasing carbon from graphite is not suitable. This also can be confirmed as the microstructure around the graphite nodules was similar to the other regions of the HAZ.

The substrate layer that is close to the interface is the PMZ in which the material is heated far above the finish austenitization temperature A_f. In the austenitic range austenite and graphite coexist and the graphite nodules release the carbon to the surrounding austenite. As a consequence, the austenite region around the graphite nodules is heavily enriched in carbon, which reduces its melting point as compared to the austenitic matrix. Accordingly, the material around the graphite nodules melts while the remaining austenite keeps its austenitic structure. During cooling, the austenite matrix is transformed to martensite which explains the martensitic matrix of the PMZ (cf. Fig. 8). Notably, the high carbon level in austenite promotes the formation of a plate-like morphology of martensite and a higher fraction of retained austenite during cooling [27]. During solidification of the melt around the graphite nodules, the carbon is absorbed from the melt to the undissolved graphite, whereby the regions close to the undissolved graphite enrich the carbon content. This gives rise to the formation of martensite during cooling forming the first shell around the graphite nodules, Fig. 9c.

The melt at a distance away from the nodule contains more carbon level than the zone close to the nodule, resulting in the formation of ledeburite during the eutectic reaction. The product of this reaction forms the second shell around the nodule [28], cf. Fig. 9f and g. The austenite component of ledeburite is not stable at room temperature and, depending on the cooling rate, is transformed into a combination of martensite, bainite and retained austenite. So, these products are observed between the cementite lamellas of the transformed ledeburite. When the entire graphite nodule dissolves in the liquid melts, see Fig. 10, the graphite nodule completely transforms to modified ledeburite during solidification.

In the first deposited layer, the melt pool is formed when the arc fuses the wire and a fraction of cast iron substrate. The intermixing of wire and substrate results in significant changes in the chemical composition and microstructure of both substrate and deposited layer. The observed narrow layer (cf. Fig. 11b indicated with red arrows) is the first region in which microstructure and chemical composition variations are

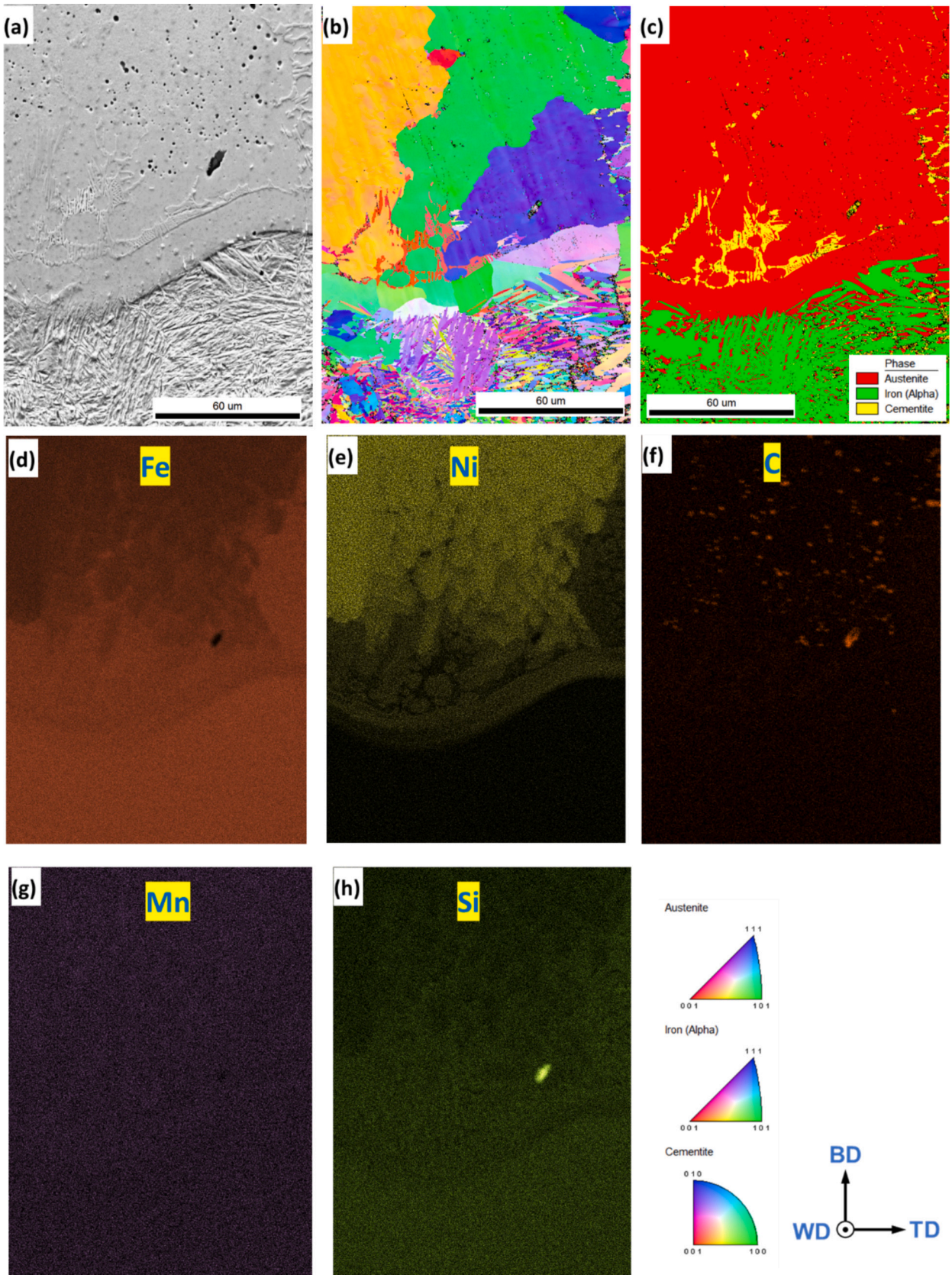

Fig. 12. (a) SEM image (b) IPF-BD map (c) phase map (d), (e), (f), (g) and (h) EDS maps taken from the PMZ/deposited alloy interface.

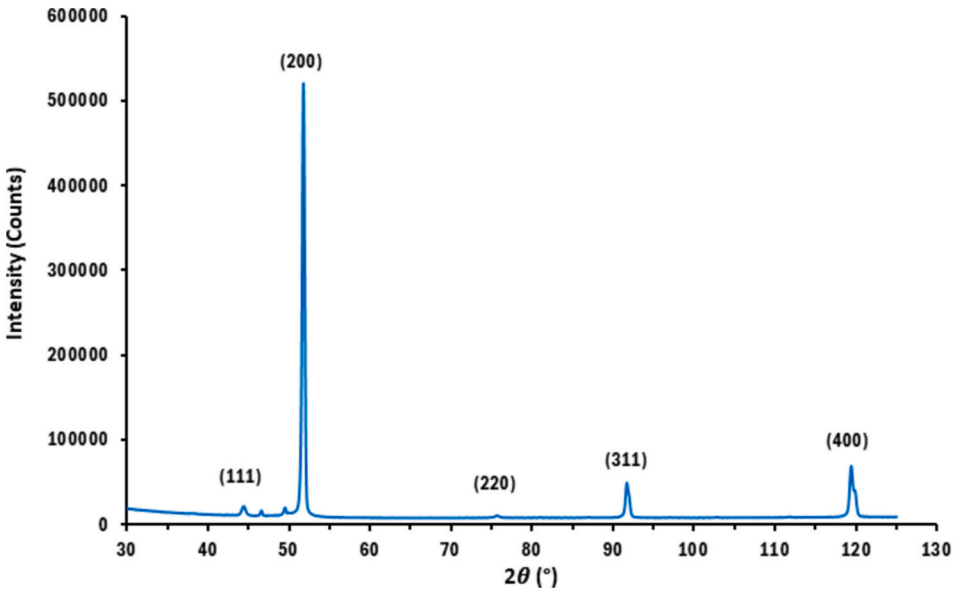

Fig. 13. The XRD results for deposited Ni-45 % Fe layers.

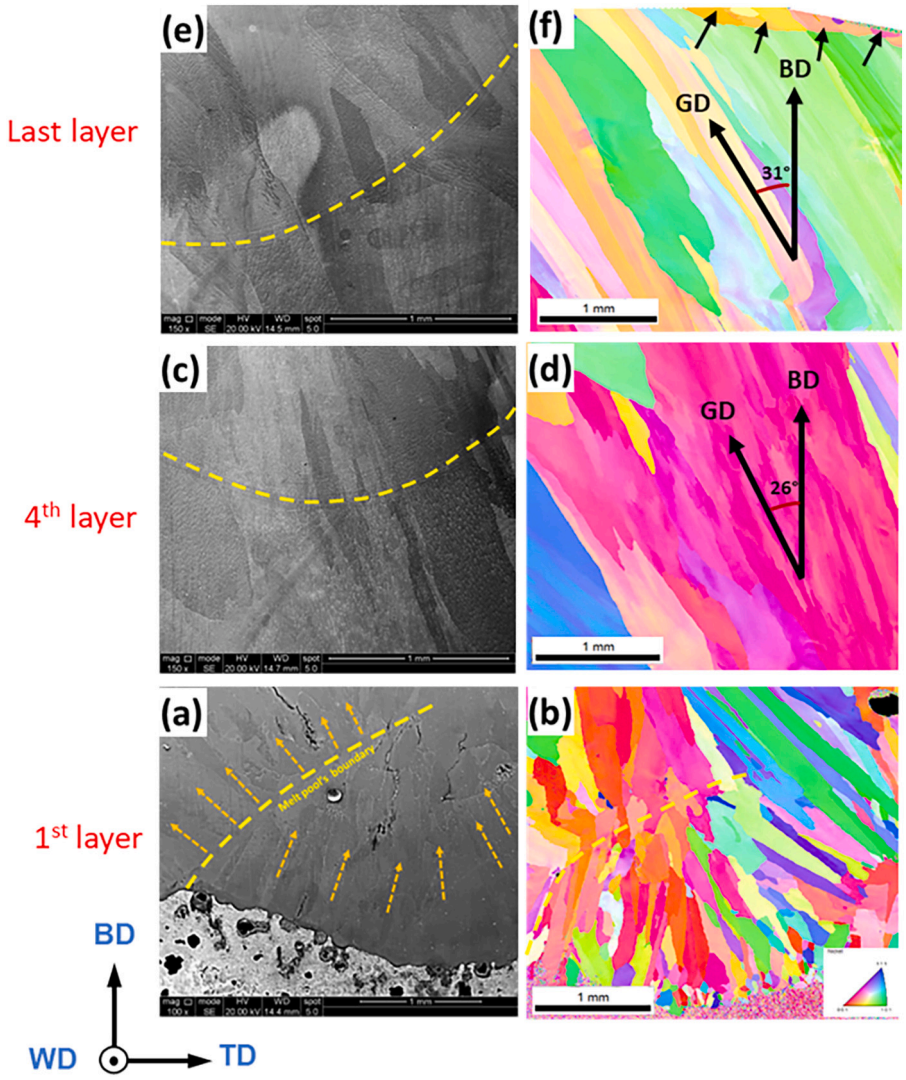

Fig. 14. Microstructure of different deposited layers (a), (c), (e) SE-SEM images (b), (d), (f) BD - IPF images.

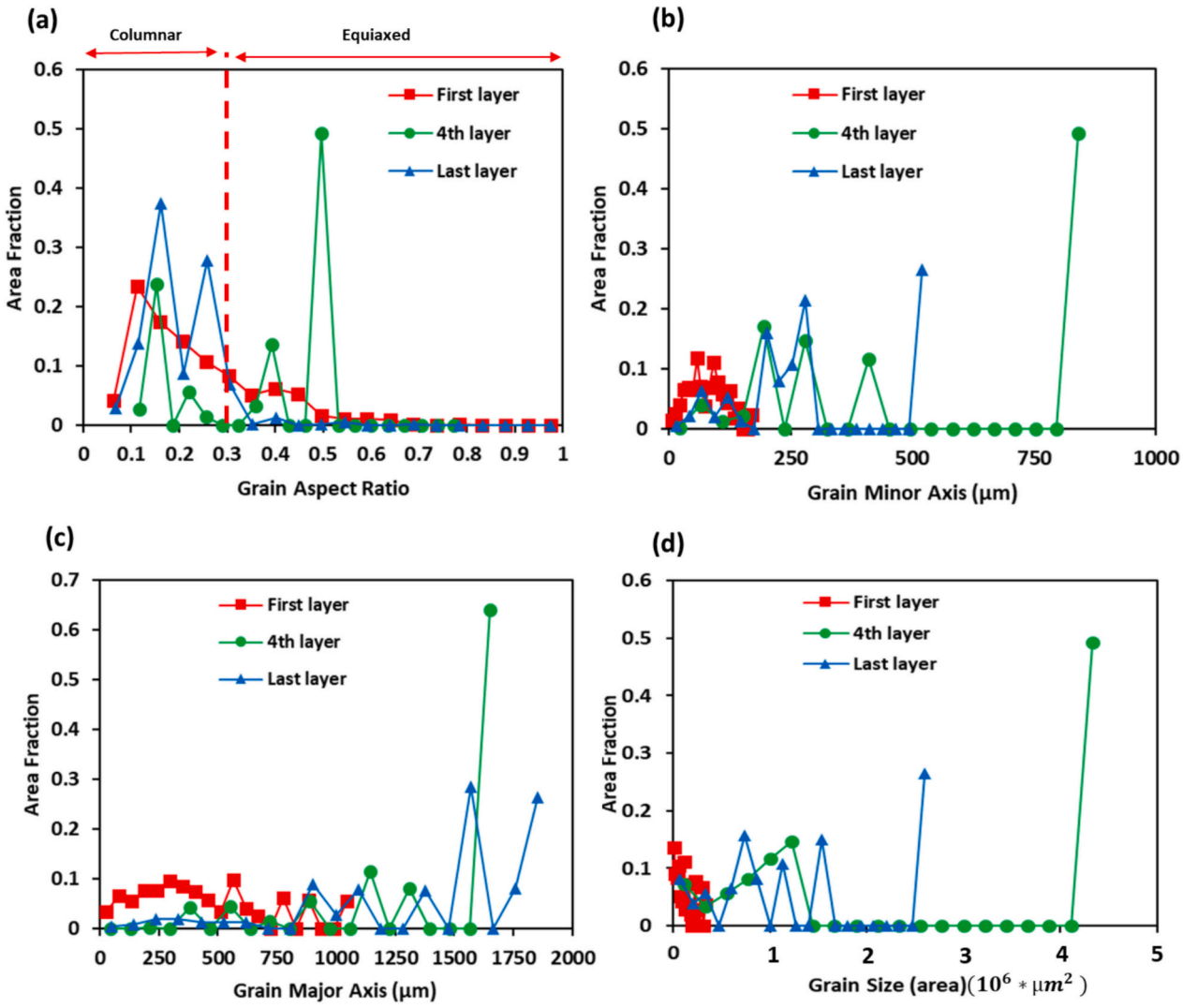

Fig. 15. The grain analysis results for different deposited layers; distribution of (a) grain aspect ratio, (b) grain minor axis, (c) grain major axis and (d) grain area.

observed. Most chemical composition variations occur within a transition zone from the interface up to 100 μm thick, where the alloying elements from both wire and substrate materials coexist. The elemental mappings reveal that the concentration profile of Ni on the one hand and of Fe and Si on the other hand, exhibit an opposite tendency; i.e. by moving away from the interface in the direction of the WAAM deposited side the Fe and Si concentration decreases, while the Ni concentration increases. These concentrational changes result from the dilution of the wire and the mixing of the wire with the substrate. The wire is composed of Ni and Fe, while Fe, Si and C are the main chemical elements of the cast iron substrate. The intermixing of wire and substrate decreases Fe and Si and increases Ni content through the transition zone. The EDS map of C reveals some concentrated regions in the transition zone that can be associated with the graphite particles that have precipitated from the melt pool during the solidification. Melting of the substrate, especially in the regions that are in contact with graphite nodules, increases the concentration of C in the melt pool. Due to the high Ni concentration in the melt pool, the solubility of carbon is very limited, whereby the extra carbon is rejected as graphite particles. This phenomenon also has been reported during the cladding of ductile cast irons with Ni rich alloys [28,29]. One of the advantages of Ni-based filler metals for welding or cladding cast irons is their ability to crystalize the absorbed carbon from the substrate in the form of graphite, increasing the crack resistance of the weld or cladded layer [17]. The elemental map of the Mn shows almost the same concentration across the interface of the bimetal sample because the initial level of Mn in both wire and substrate is almost the same.

Considering Fig. 12 and Fig. 14, the solidification of the first deposited layer starts with the formation of a narrow layer at the fusion boundary. The development of this layer is related to the dominance of planer growth of FCC phase with the onset of the solidification of the melt pool. The presence of a high temperature gradient (G) and low growth rate (R) at the fusion boundary dominates the planar growth mode [30]. By moving away from the fusion boundary, the ratio of G/R decreases, whereby the planar solidification is replaced by the cellular solidification mode, see Fig. 19.

The development of such cellular structure during WAAM has also been reported by other researchers [31] [32].

It was observed that <100> II BD is the predominant texture for different heights of the deposited material. However, a rotation from the BD was observed in the pole figures. The crystal growth from the liquid phase usually occurs in the directions perpendicular to the liquidus isotherms, as these directions have the steepest temperature gradients. It is important to consider that crystal growth is not isotropic; some directions are preferred over others for crystal growth [33]. For example, the <100> directions are the preferred crystallographic growth directions in metals with FCC and BCC crystal structures. Because the crystallization occurs from the liquid atoms having a random

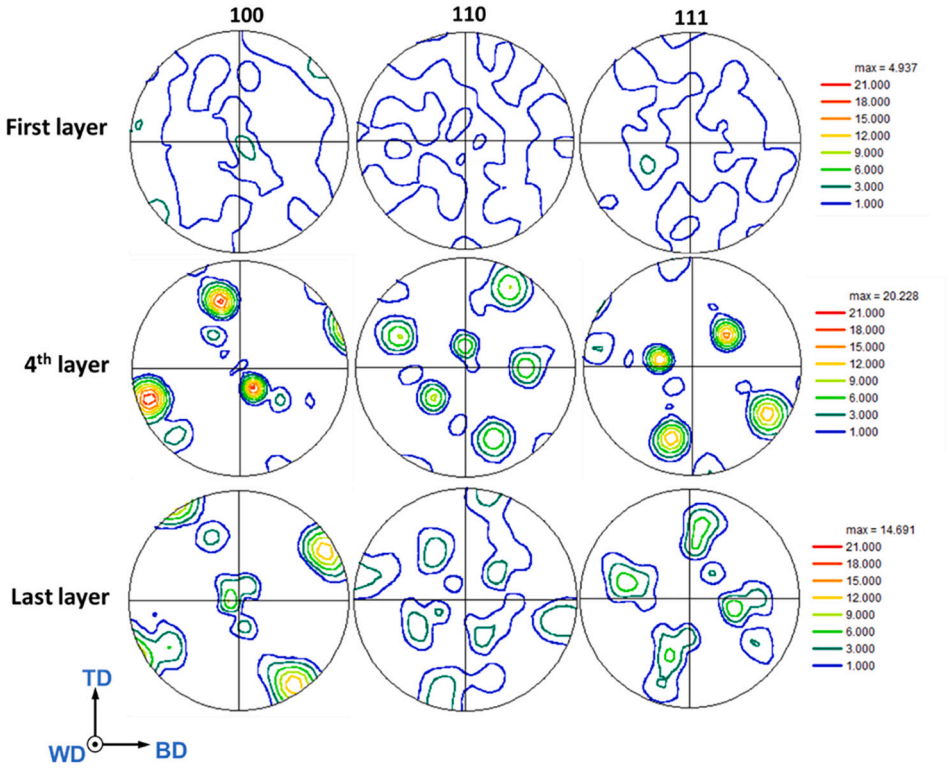

Fig. 16. Pole figures related to different deposited layers of Ni-45 %Fe alloy.

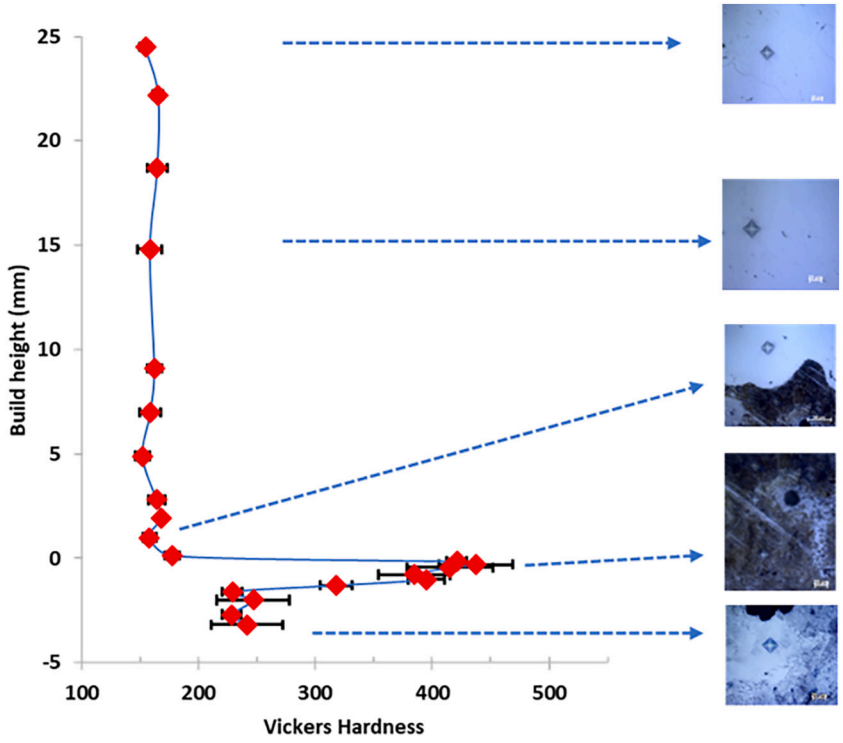

Fig. 17. Hardness profile of the bimetallic structure.

arrangement, the deposition of atoms in the least closed packed direction, e.g. <100> direction, provides a higher growth rate than the other denser directions. So, considering both heat transfer and crystallographic features, the crystal growth occurs in <100> directions closest to the largest temperature gradients [34]. It must be stressed, though, that temperature conductivity q is not an anisotropic property in cubic metals and therefore, in itself is not the reason for the anisotropic crystal growth. The temperature gradients are determined by the shape and geometry of the melt pool. Using the tracing of fusion boundaries in the DB-TD cross section, Fig. 2a, a mean shape of the melt pool could be

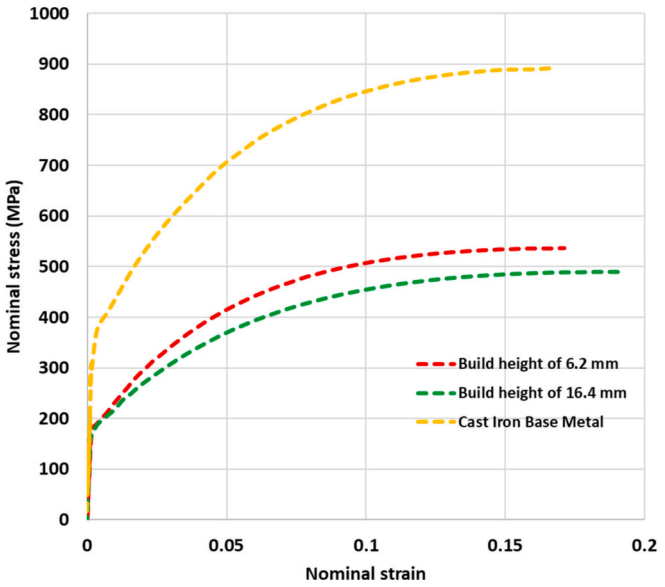

Fig. 18. Nominal stress-strain curves generated from the PIP studies.

Table 3
Tensile properties obtained from profilometry-based indentation plastometry (PIP) measurements.

Location of the indent	Yield strength (MPa)	Ultimate tensile strength (MPa)	Uniform elongation (%)
Cast Iron-base metal	355	895	17.5
Point 1 on Ni—Fe alloy (height of 6.23 mm)	172	536	17.4
Point 2 on Ni—Fe alloy (height of 16.46 mm)	171	494	20.2
As welded Ni—Fe alloy *	230	400	24

* Indicates the mechanical properties of the as-welded Ni—Fe alloy obtained from the supplier datasheet.

obtained, cf. Fig. 20.

It is seen that the dimensions of the melt pool closely match the spaces between parallel beads (3.25 mm) and between vertical layers (2.5 mm) during the deposition process. It should be noted that the shape of the fusion zone is determined by the manufacturing conditions. It was observed that large columnar grains have formed with a deviation from the building direction, see Fig. 14. This deviation is consistent with a rotation of the <100> fibre in the (100) PFs from the building direction. This rotation in crystallographic texture corresponds to the angular deviation of the maximum temperature gradient from the building direction. A large portion of heat during WAAM is transferred using conductive heat flow through the materials surrounding the melt pool. A solidifying melt pool is in contact with the underneath solidified layer and the previously deposited track next to it, meaning that conductive heat flow takes place with an angular deviation to the building direction.

The variation of the micro-hardness across the interface is related to the microstructural gradient. It was observed that the base metal has a pearlitic matrix, while the development of HAZ and PMZ regions results in the formation of microstructures with different matrix. Increasing the hardness in the matrix of HAZ, compared with base metal, is mainly due to the formation of fine pearlitic structure as well the presence of martensite between the cementite lamellas (see Fig. 7). The refinement of the pearlitic structure results in lowering cementite interlamellar spacing, which decreases the mean free path for dislocation motions and, in turn, increases hardness [35]. Refining the pearlitic structure also generates a higher density of cementite/ferrite boundaries, acting as an obstacle against dislocation movement and increasing strength or hardness [36]. Formation of the hard phase of martensite between the cementite lamellas also reduces the mean free path for dislocation motion, thereby increasing the hardness of the HAZ. Peak hardness was observed in PMZ mainly due to the formation of a high carbon plate martensitic structure in this region. The high hardness of martensite plates in highly alloyed martensitic steels with reduced Stacking- Fault Energy results from thier unique sub-sractural features, including the formation of ultrafine twins within a high-density dislocation matrix. [37].

There is a sharp decrease in the hardness of deposited Ni—Fe alloy compared to the PMZ in the cast iron side due to the changing microstructure from high carbon martensite into Ni—Fe austenitic structure (see Fig. 13). This lower hardness/strength could be due to the lower amount of carbon in the Ni—Fe austenitic structure. It has been shown that carbon, as an interstitial alloying element, has a much larger effect on the hardening of austenite than substitutional elements such as nickel [38]. The first deposited layer's initial region has a higher hardness (10

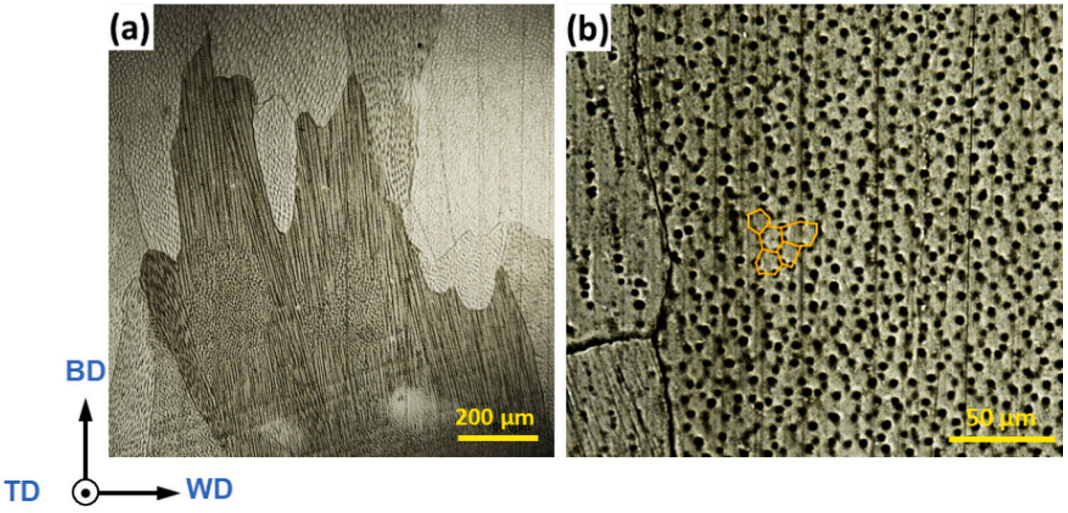

Fig. 19. Formation of cellular solidification structure in deposited Ni-45 %Fe alloy.

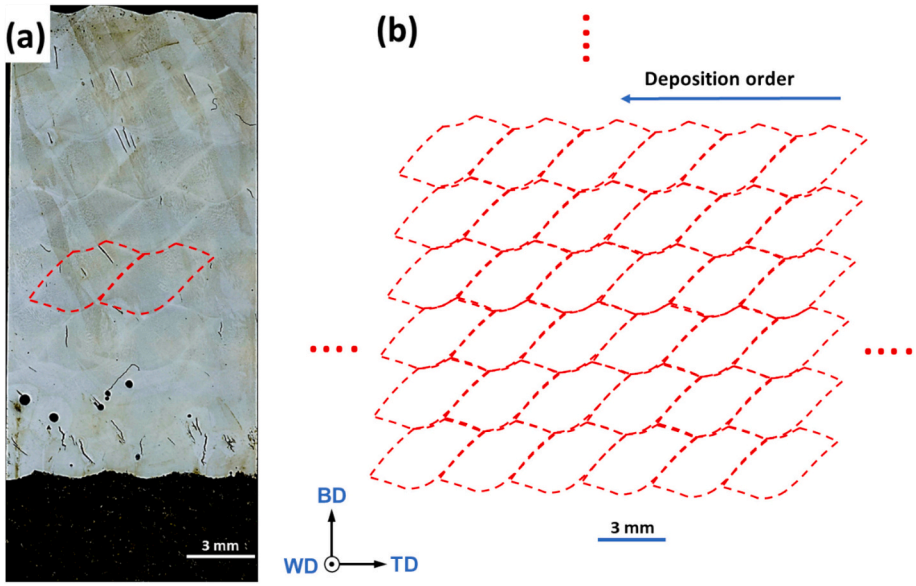

Fig. 20. (a) Mean shape of the melt pool extracted by tracing the fusion boundaries and (b) schematic representation of the melt pools converting to the deposited solid material.

%) than the other deposited layers, which is due to the lower grain size of austenite in the layer on top of the interface. It is worth mentioning that the hardness of deposited Ni—Fe alloy is in the range of the value (150 HV) reported by the wire supplier.

The PIP results also confirm the micro-hardness measurements where the σ_y and the *UTS* of deposited alloy are much lower than the cast iron base metal (see Fig. 18). Besides the investigation of stress-strain behaviour, PIP testing can also provide some insights into the presence of plastic anisotropy. In the case of in-plane isotropy, the profile of the indent is radially symmetric. Fig. 21 shows a micrograph of indent corresponding to the build height of 6.3 mm in Ni—Fe alloy.

The measurement of the diameters reveals that the indent profile is radially asymmetric meaning that there are in-plane directions which are softer than other directions. This can be interpreted as an obvious in-plane anisotropy which is in line with texture results showing highly textured microstructure in deposited alloy.

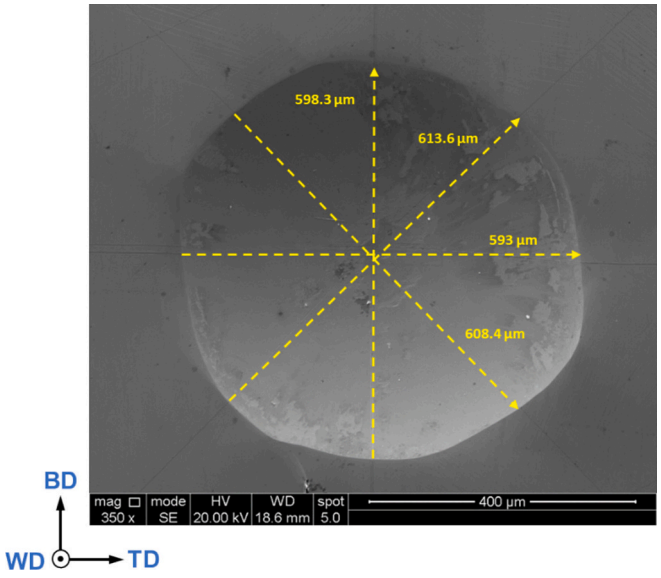

Fig. 21. Scanning electron microscopy (SEM) image of indent corresponding indent profile at build height of 6.3 mm in Ni—Fe alloy.

5. Summary and conclusions

In the present research, a hybrid structure of Ni-45 %Fe alloy/ductile cast iron was fabricated using the printing of Ni-45 %Fe alloy on a ductile cast iron substrate. The interfacial region and deposited alloy were characterized using SEM, EBSD, EDS and XRD techniques. The following can be concluded:

1) The region within which the main compositional and microstructural changes occur can be divided into heat affected zone, partially melted zone and the first deposited layer;

   i) The microstructure of heat affected zone consists of initial graphite and cementite distributed in a partially decomposed pearlitic structure with additionally, martensite, ferrite, and retained austenite.
   ii) The partially melted zone features a martensitic matrix, ledeburite, and graphite particles surrounded by shells of martensitic, bainitic and transformed ledeburitic microstructure.
   iii) In the first deposited layer, the matrix has an austenitic structure. Additionally, solidification of the cementite network and graphite particles are observed in regions close to the interface. The deposited Ni-45 %Fe alloy shows a fully austenitic structure.

2) The dilution effect was evident in the first deposited layer due to intermixing of the wire and the substrate, whereby the migration of Ni, Fe, C and Si alloying elements occurs.
3) The evolution of pole figures on different deposited layers showed that the texture of the deposited alloy revealed some deviations from the expected <100> parallelism to the building direction. It was revealed that this deviation is related to the deviation of heat extraction direction from the building direction due to the shape and overlap of the melt pools.
4) Some cracks and pores have been formed within the interface and deposited alloy. Further studies are required to understand their origin and develop processing strategies aimed to avoid these deficiencies.
5) The peak of the hardness across the interface was observed in PMZ because of the formation of a martensitic matrix. The profilometry-based indentation plastometry (PIP) measurements showed that

the σ_y and the *UTS* of the deposited alloy are lower than those of the cast iron base metal.

CRediT authorship contribution statement

Mahdi Mahmoudiniya: Writing – original draft, Methodology, Investigation, Data curation, Conceptualization. **Anne-Sophie Thorr:** Writing – review & editing, Project administration. **Roumen H. Petrov:** Writing – review & editing, Visualization, Supervision, Methodology, Investigation, Formal analysis, Conceptualization. **Marcel J.M. Hermans:** Writing – review & editing, Project administration, Funding acquisition, Conceptualization. **Leo A.I. Kestens:** Writing – review & editing, Visualization, Supervision, Project administration, Methodology, Funding acquisition, Formal analysis.

Declaration of competing interest

The authors declare that they have no known competing financial interests or personal relationships that could have appeared to influence the work reported in this article.

Data availability

The raw data required to reproduce these findings cannot be shared at this time because the data also forms part of an ongoing study. However, the authors are open to sharing any particular data on request.

Acknowledgement

This research was carried out within the project “Grade2XL - Functionally Graded Materials for Extra Large Structures”, which has received funding from the European Union’s Horizon 2020 research and innovation program under grant agreement No 862017.

References

[1] R. Singh, Cast iron and cast steel: Applied Welding Engineering, Elsevier (2020) 61–76, https://doi.org/10.1016/B978-0-12-821348-3.00020-3.
[2] Chapter-6—Ductile-iron_2000_Foseco-Ferrous-Foundryman-s-Handbook.pdf, (n. d.).
[3] J.P. Oliveira, T.G. Santos, R.M. Miranda, Revisiting fundamental welding concepts to improve additive manufacturing : from theory to practice, Prog. Mater. Sci. 107 (2020) 100590, https://doi.org/10.1016/j.pmatsci.2019.100590.
[4] A. Review, Wire arc additive manufacturing of stainless steels, Appl. Sci. (2020), https://doi.org/10.3390/app10051563.
[5] A. Vahedi, M. Ghaffari, S. Salahi, A. Nasiri, Effects of post-printing heat treatment on the microstructure and mechanical properties of a wire arc additive manufactured 420 martensitic stainless steel part, Mater. Sci. & Eng. A 813 (2021) 141167, https://doi.org/10.1016/j.msea.2021.141167.
[6] K.E.K. Vimal, M. Naveen Srinivas, S. Rajak, Wire arc additive manufacturing of aluminium alloys: a review, Materials Today: Proceedings 41 (2021) 1139–1145, https://doi.org/10.1016/j.matpr.2020.09.153.
[7] V. Dhinakaran, J. Ajith, A. Fathima Yasin Fahmidha, T. Jagadeesha, T. Sathish, B. Stalin, Wire Arc Additive Manufacturing (WAAM) process of nickel based superalloys – A review, Materials Today: Proceedings 21 (2020) 920–925, https://doi.org/10.1016/j.matpr.2019.08.159.
[8] R. Chen, C. Tan, Y. Yu, M. Zhang, X. Yu, C. Liu, Modification of α-phase of wire + arc additive manufactured Ti-6Al-4 V alloy with boron addition, Mater. Charact. 169 (2020) 110616, https://doi.org/10.1016/j.matchar.2020.110616.
[9] Microstructure and mechanical properties of NiTi-SS bimetallic structures built using Wire Arc Additive Manufacturing, (n.d.). doi:https://doi.org/10.1016/j.matlet.2021.130499.
[10] F. Marefat, J. De Pauw, A. Kapil, N. Chernovol, P. Van Rymenant, A. Sharma, Design strategies for bi-metallic additive manufacturing in the context of wire and arc directed energy deposition, Mater. Des. 215 (2022) 110496, https://doi.org/10.1016/j.matdes.2022.110496.
[11] C. Dharmendra, S. Shakerin, G.D.J. Ram, M. Mohammadi, Wire-arc additive manufacturing of nickel aluminum bronze/stainless steel hybrid parts – interfacial characterization, prospects, and problems, Materialia 13 (2020) 100834, https://doi.org/10.1016/j.mtla.2020.100834.
[12] N. Hasani, M.H. Ghoncheh, R.M. Kindermann, H. Pirgazi, M. Sanjari, S. Tamimi, S. Shakerin, L.A.I. Kestens, M.J. Roy, M. Mohammadi, Dislocations mobility in superalloy-steel hybrid components produced using wire arc additive manufacturing, Mater. Des. 220 (2022) 110899, https://doi.org/10.1016/j.matdes.2022.110899.
[13] R. Sebastian, A.K. Singh, M. Paliwal, A. Gautam, Investigation of the interface between SLM processed nickel alloy on a cast iron substrate, Progress Additiv. Manuf. 4 (2019) 131–142, https://doi.org/10.1007/s40964-018-0066-y.
[14] D. Samantaray, B. Aashranth, N.L. Parthasarathi, A.K. Rai, M.A. Davinci, C.P. Paul, U. Borah, K.S. Bindra, S.K. Albert, A.K. Bhaduri, Assessing the co-deformability of a nickel-based Superalloy-304L stainless steel preform manufactured through laser additive manufacturing, J. Mater. Eng. Perform. 30 (2021) 6667–6672, https://doi.org/10.1007/s11665-021-05951-6.
[15] F. Veiga, A. Suárez, T. Artaza, E. Aldalur, Effect of the heat input on wire-arc additive manufacturing of invar 36 alloy: microstructure and mechanical properties, Weld World 66 (2022) 1081–1091, https://doi.org/10.1007/s40194-022-01295-4.
[16] A. Sood, J. Schimmel, V.M. Ferreira, M. Bosman, C. Goulas, V. Popovich, M.J. M. Hermans, Directed energy deposition of invar 36 alloy using cold wire pulsed gas tungsten arc welding: effect of heat input on the microstructure and functional behaviour, J. Mater. Res. Technol. 25 (2023) 6183–6197, https://doi.org/10.1016/j.jmrt.2023.06.280.
[17] M. Pouranvari, On the weldability of grey cast iron using nickel based filler metal, Mater. Des. 31 (2010) 3253–3258, https://doi.org/10.1016/j.matdes.2010.02.034.
[18] R.M. Nunes, B.L. Alia, R.L. Alley, W.R. Apblett, W.A.B. III, W. Ballis, C.C. Bampton, P. Banerjee, J.G. Banker, R.G. Bartifay, R.I. Batista, R.E. Beal, R.E. Bohlmann, S.D. Brandi, J.A. Brooks, D.W. Bucholz, P. Burgardt, R.A. Bushey, C. Cable, R.D. Campbell, H. Cary, H. Castner, A. Cedilote, H.A. Chambers, C.C. Chen, S. Chen, S.-P. Chen, B.A. Chin, M.J. Cieslak, R.E. Cook, S.A. Coughlin, M. Cowell, R.S. Cremisio, C.E. Cross, C. Dallam, B. Damkroger, J.R. Davis, WELDING, BRAZING, AND SOLDERING, n.d.
[19] T.W. Clyne, J.E. Campbell, M. Burley, J. Dean, Profilometry-based inverse finite element method indentation Plastometry, Adv. Eng. Mater. 23 (2021) 2100437, https://doi.org/10.1002/adem.202100437.
[20] M. Godec, S. Zaefferer, B. Podgornik, M. Šinko, E. Tchernychova, Quantitative multiscale correlative microstructure analysis of additive manufacturing of stainless steel 316L processed by selective laser melting, Mater. Charact. 160 (2020) 110074, https://doi.org/10.1016/j.matchar.2019.110074.
[21] D. Jafari, T.H.J. Vaneker, I. Gibson, Wire and arc additive manufacturing: opportunities and challenges to control the quality and accuracy of manufactured parts, Mater. Des. 202 (2021) 109471, https://doi.org/10.1016/j.matdes.2021.109471.
[22] Department of Manufacturing Engineering Technology, College of Technological Studies, public Authority for Applied Education & Training, Kuwait., A.I. Albannai, A Brief Review on The Common Defects in Wire Arc Additive Manufacturing, Ijcsrr 05, 2022, https://doi.org/10.47191/ijcsrr/V5-i12-19.
[23] C. Labrecquee, M. Gagne, DUCTILE IRON: FIFTY YEARS OF CONTINUOUS DEVELOPMENT, Can. Metall. Q. 37 (1998) 343–378.
[24] S. Lee, J. Kim, D.S. Shim, S.H. Park, Y.S. Choi, Micro-cracking in medium-carbon steel layers additively deposited on gray cast Iron using directed energy deposition, Met. Mater. Int. 26 (2020) 708–718, https://doi.org/10.1007/s12540-019-00589-5.
[25] S. Biggin, D.J. Dingley, A general method for locating the X-ray source point in Kossel diffraction, J. Appl. Crystallogr. 10 (1977) 376–385, https://doi.org/10.1107/S0021889877013806.
[26] A. Hadadzadeh, B.S. Amirkhiz, J. Li, M. Mohammadi, Columnar to equiaxed transition during direct metal laser sintering of AlSi10Mg alloy: effect of building direction, Addit. Manuf. 23 (2018) 121–131, https://doi.org/10.1016/j.addma.2018.08.001.
[27] G. Krauss, A.R. Marder, The morphology of martensite in iron alloys, Metall. Trans. A. 2 (1971) 2343–2357, https://doi.org/10.1007/BF02814873.
[28] Y. Li, S. Dong, S. Yan, P. He, B. Xu, Phase evolution of ductile iron during laser cladding processing, Surf. Coat. Technol. 339 (2018) 37–47, https://doi.org/10.1016/j.surfcoat.2018.02.011.
[29] Y. Li, S. Dong, P. He, S. Yan, E. Li, X. Liu, B. Xu, Microstructure characteristics and mechanical properties of new-type FeNiCr laser cladding alloy coating on nodular cast iron, J. Mater. Process. Technol. 269 (2019) 163–171, https://doi.org/10.1016/j.jmatprotec.2019.02.010.
[30] C. John, lippold, Welding Metallurgy and Weldability, 2014.
[31] W. Chen, Y. Chen, T. Zhang, T. Wen, X. Feng, L. Yin, Effects of location on the microstructure and mechanical properties of cu-8Al-2Ni-2Fe-2Mn alloy produced through wire arc additive manufacturing, J. Mater. Eng. Perform. 29 (2020) 4733–4744, https://doi.org/10.1007/s11665-020-04955-y.
[32] W. Zhang, Y. Lei, W. Meng, Q. Ma, X. Yin, L. Guo, Effect of deposition sequence on microstructure and properties of 316L and Inconel 625 bimetallic structure by wire arc additive manufacturing, J. Mater. Eng. Perform. 30 (2021) 8972–8983, https://doi.org/10.1007/s11665-021-06137-w.
[33] K. Easterling, The weld metal, in: Introduction to the Physical Metallurgy of Welding, Elsevier, 1992, pp. 55–125, https://doi.org/10.1016/b978-0-7506-0394-2.50007-1.
[34] S. Suwas, R.K. Ray, Crystallographic Texture of Materials, Springer London, London, 2014, https://doi.org/10.1007/978-1-4471-6314-5.
[35] A.M. Elwazri, P. Wanjara, S. Yue, The effect of microstructural characteristics of pearlite on the mechanical properties of hypereutectoid steel, Mater. Sci. Eng. A 404 (2005) 91–98, https://doi.org/10.1016/j.msea.2005.05.051.
[36] Y. Mu, P. Xu, Y. Liang, S. Xiang, C. Yin, Improving the tensile ductility in the fully pearlitic steel using sequential refinement of colony and laminated structure,

Mater. Sci. Eng. A 851 (2022) 143642, https://doi.org/10.1016/j.msea.2022.143642.
[37] J. Wang, Q. Tao, J. Fan, L. Fu, A. Shan, Enhanced mechanical properties of a high-carbon martensite steel processed by heavy warm rolling and tempering, Mater. Sci. Eng. A 872 (2023) 144958, https://doi.org/10.1016/j.msea.2023.144958.
[38] G. Badinier, C.W. Sinclair, S. Allain, F. Danoix, M. Gouné, The mechanisms of transformation and mechanical behavior of ferrous Martensite, in: Reference Module in Materials Science and Materials Engineering, Elsevier, 2017, https://doi.org/10.1016/B978-0-12-803581-8.02518-2. B9780128035818025182.